

Thermal expansion behavior and elevated temperature elastic properties of an interpenetrating metal/ceramic composite

Joél Schukraft ^{a,*}, Jan Roßdeutscher ^b, Frederik Siegmund ^a, Kay A. Weidenmann ^a

^a Hybrid Composite Materials, Institute of Materials Resource Management, Augsburg University, Am Technologiezentrum 8, 86159 Augsburg

^b Institute of Materials Research, German Aerospace Center (DLR), Linder Höhe, 51147 Cologne, Germany

1. Introduction

Amidst the global challenge of climate change, the careful use of our environment and its resources is becoming increasingly relevant. Lightweight design and the development of new materials with improved properties and reduced weight are considered key enabling technologies to facilitate energy and CO₂ savings, especially in the mobility and transport sector. However, conventional lightweight metals have widely reached their limits with regards to their mechanical and thermal properties. Therefore, new material concepts such as composite materials have to be considered for more demanding applications. Among various types of composite materials, interpenetrating phase composites (IPCs) or more specifically interpenetrating metal ceramic composites (IMCCs) have been suggested to offer various benefits and improved thermo-mechanical properties over conventional lightweight metals [1].

IMCCs are typically made of an open porous ceramic preform body that acts as a reinforcement and a metal matrix. A metallic melt is infiltrated into the porous ceramic preform by means of pressure die casting [1,2] gas pressure infiltration [3,4], squeeze casting [5], or pressureless infiltration [6,7], depending on the morphological

properties of the preform such as pore size and the proportions of closed and open porosity. Local reinforcement can thus increase the mechanical properties without substantially increasing the density of the material.

One example is the interpenetrating aluminum-alumina composite studied in this paper. The alumina preform of the IMCC used in this work was fabricated by mechanical foaming [8]. Alternative manufacturing methods for the preform of an aluminum-alumina IMCC include freeze casting [9,10], sintering of coarse alumina powders into an open-pore ceramic [11], or pore-forming processes using carbon fibers [12], wax [13] or starch [14] as placeholders, which are subsequently pyrolyzed.

IMCCs have higher compressive strength and stiffness than metallic materials [15,16]. They feature a higher fracture toughness and are more ductile compared to other composites due to the high ductility of the metal component, i.e., they can absorb large impact fracture energies [17]. The combination of the soft alloy and the hard ceramic results in high wear resistance [18,19]. Since the ceramic impedes thermal expansion, it is significantly lower compared to the matrix metal of the composite [20]. This also influences the internal stress distribution during manufacturing and in operation, as Roy et al. investigated

* Correspondence:

E-mail addresses: joel.schukraft@mrm.uni-augsburg.de (J. Schukraft), jan.rossdeutscher@dlr.de (J. Roßdeutscher).

intensively [21–25]. Load transfer takes place from the softer to the stiffer phase. In an interpenetrating AlSi12/alumina composite with 40 % alumina phase, the longitudinal stress in the alumina phase is circa the double under tension and compression, compared with the aluminum phase [21]. The aluminum phase only takes half of the applied stress with a decreasing value due to plasticity [24]. In Roy et al. [22] the effect of phase architecture on the mechanical properties was investigated and showed for different morphologies (placeholder foam based and lamellar by freeze-casting) that anisotropic strengthening takes place by carrying up to 90 % of the applied stress in the alumina phase. Another effect in metal matrix composites, also relevant for the investigated IMCC, is microcracking and its impact on the elastic modulus. In resonant ultrasonic spectroscopy measurements over a temperature profile with a constant change in temperature, PbTe and PbS with SiC nanoparticles develop a hysteresis when comparing heating and cooling cycles at T_{\max} close to melting, due to microcracks which anneal at high temperature when the metal plasticizes and open up again during cooling [27]. A similar effect was shown by Castillo-Hernandez et al. in Mg2Si and Mg2Sn specimens investigated with the impulse excitation technique at a temperature up to 410°C with a heating and cooling rate of 5 K/min and a dwell time of 30 min. All investigated samples exhibit a linear decrease in elastic properties with increasing temperature. After reaching the dwell time, a small increase in elastic modulus <1 % takes place, which leads to a hysteresis. As an integrity check, it is supposed to confirm, that the initial value for the elastic modulus is reached again at room temperature after the thermal cycle [28].

As Roy et al. [26] investigated for an Al12Si/alumina IMCC, the interfacial bond strength is inherently strong. During manufacturing, process induced thermal residual stress is brought into the composite. Generally, residual tensile stresses are built up in the metallic phase and residual compression stresses are built up in the ceramic phase [27]. Therefore, the first heating cycle is not considered for thermal expansion by different authors. Experiments on thermal expansion for interpenetrating phase composites have been conducted by Balch et al. [28], Skirl et al. [11] and Roy et al. [29]. The typical heating curves from the second cycle onwards show a strong constant increase in strain up to a transition temperature, where the metal starts to plasticize. Here the curve bends to a lower slope. The reason for this thought to be the metal plasticizing at the kink and flowing into voids, created by imperfect infiltration. This stress relief is then reflected in the significantly lower slope of the strain-temperature-curve. From this plasticizing point on, the metal phase no longer contributes to the strain, since it can flow, unlike the ceramic preform. Experiments were conducted with a SiC preform infiltrated with aluminum [28]. The same effect was shown by Skirl et al. for aluminum-alumina IMCCs. Furthermore, they showed, that due to this behavior, the coefficient of thermal expansion (CTE), which is the derivative of the strain, exhibits a similar effect. For a composite with an aluminum volume content of 65 %, the CTE in the first phase rises from 13 to a peak of $16 \cdot 10^{-6} \text{ K}^{-1}$ at about 300°C before dropping to values around 7 to $9 \cdot 10^{-6} \text{ K}^{-1}$ at about 450°C [11]. Roy et al. [29] studied IMCCs with 34 to 60 % ceramic content. The thermal strain and CTE were investigated in a temperature range between room temperature and 500°C with a heating rate of 5 K/min. The composites have shown a manufacturing related thermal anisotropy. The thermal anisotropy is directly related to the elastic behavior. Thermal expansion decreased with increasing ceramic content. For the given studies, the range relation for thermal expansion was only investigated from room temperature to one maximum temperature. For repeated heating cycles, a decrease of residual stress within the composites was observed. Nevertheless, the effect of residual stress relief, different maximum temperatures and the physical phenomena behind the variation of CTE with temperature have not been investigated yet. Also, the combination of dilatometry experiments with elastic modulus measurements, to investigate the identical phenomena behind, is described the first time in literature, for the best knowledge of the authors.

For the application of IMCCs in a thermal environment, this relation is relevant for the understanding of the mechanisms within the material, as well as the investigation of the thermal dependencies of the elastic modulus.

Therefore, this study investigates the behavior of the thermal expansion coefficient, and the elastic properties in an interpenetrating aluminum-alumina composite at room temperature, and the influence of elevated temperature on the material properties.

2. Materials and Methods

2.1. Materials and sample preparation

Previous studies on this material system were carried out regarding microstructure, residual porosity and mechanical characterization and can be found in [30–33]. Based on these, the material processing is described in the following:

A highly porous open-cell alumina ceramic preform with a relative density of approximately 26 vol.-% is used in this study. It was produced by Morgan Advanced Materials Haldenwanger GmbH, Waldkraiburg, Germany, which holds a patent on the preform manufacturing process [8]. To get a highly homogeneous ceramic preform, a stable ceramic foam suspension is produced by mechanical stirring in a slurry-based processing route. The use of additives and a well-engineered drying process makes molding and drying of the green body possible, without losing the fine and homogeneous distributed porosity. The ceramic foam is finally produced by sintering.

A gas-pressure infiltration process with an AlSi10Mg alloy was used to manufacture the IMCC. In an evacuated vacuum vessel at a residual pressure of maximum $2 \cdot 10^{-2}$ mbar, the ceramic preform was heated up to 700°C together with AlSi10Mg slabs. After melting of the slabs surrounding the ceramic foam, an external Argon gas pressure of 60 bar was applied onto the surface of the melt bath. For a short dwell time of 10 min the temperature was held, and the chamber then cooled down to room temperature under the remaining Argon pressure. The solidified interpenetrating composite block was finally removed from the pressurized vessel for sample preparation. Details and a schematic drawing of the process setup are described by one of the authors in Horny et al. [30]. Images of the bulk and microstructure of the ceramic preform as well as the microstructure of the interpenetrating phase composite are shown in Fig. 1.

Samples of the ceramic foam, the AlSi10Mg alloy and the IMCC were prepared for the respective analysis by cutting with a diamond wire-saw by diamond wiretec, Weinheim, Germany. The samples surfaces were ground with SiC grinding paper stepwise from P320 to P800. The final dimensions of the samples were measured with Tesa- μ -hite, by Hexagon, Stockholm, Sweden. For ultrasonic phase spectroscopy (UPS), the samples had a size of ca. $10 \times 10 \times 10 \text{ mm}^3$. For the investigation of the resonant frequency damping analysis (RFDA), the samples were cut to rectangular bars with a geometry of ca. $60 \times 10 \times 4 \text{ mm}^3$. The samples for the dilatometry experiments were cut to a final size of ca. $5 \times 5 \times 25 \text{ mm}^3$.

2.2. Ultrasonic phase spectroscopy

The elastic constants were determined with ultrasonic phase spectroscopy (UPS) method by nondestructive testing, as already presented in a previous study (cf. Horny et al. [30]):

Continuous sinusoidal waves are emitted by a transducer and propagate through the investigated material. The occurring phase shift is measured over a frequency range. Such a wave can be written as:

$$u(x, t) = u_0 e^{i(\omega t + kx)} \quad (1)$$

Whereby ω is the angular frequency ($\omega = 2\pi f$) and k is the wave number ($k = 2\pi/f$). The group velocity U of these waves can be determined for a

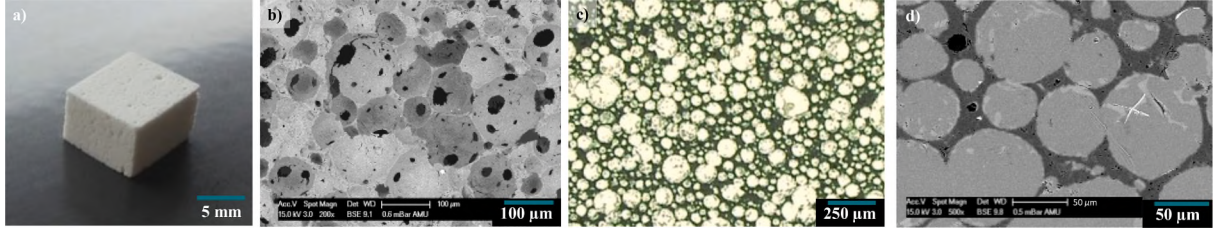


Fig. 1. Images of the alumina preform and the interpenetrating metal ceramic composite. a) Photo of the macroscopic structure of the open porous alumina foam. b) SEM image of the foam microstructure with its open cells, connected by apertures to each other. Scanning parameters are given in the info bar in the image. c) Light microscopy image of the infiltrated microstructure. The light and round shaped parts represent the metallic phase infiltrated into the open porous structure. The surrounding dark phase is the alumina ceramic. Darker grey parts within the metallic phase represent precipitations of the AlSi10Mg. d) High-resolution SEM image of the local microstructure, precipitations, closed porosity in the ceramic foam and infiltration faults within the metallic phase.

frequency sweep from the incremental ratio of the phase difference $\Delta\phi$ and the frequency f and the known sample thickness L , as:

$$U = \frac{2 \cdot \pi \cdot L}{\frac{d\Delta\phi}{df}} \quad (2)$$

Thus, if the slope of the phase-frequency plot consisting of the phase difference $\Delta\phi$ and the frequency f is continuous, the corresponding elastic constant can be determined in dependance of the density as ρ , [34,35]:

$$C_{11} = \rho \cdot U_{11}^2 \quad (3)$$

$$C_{22} = \rho \cdot U_{22}^2 \quad (4)$$

$$C_{33} = \rho \cdot U_{33}^2 \quad (5)$$

$$C_{44} = \rho \cdot U_{23}^2 = \rho \cdot U_{32}^2 \quad (6)$$

$$C_{55} = \rho \cdot U_{13}^2 = \rho \cdot U_{31}^2 \quad (7)$$

$$C_{66} = \rho \cdot U_{12}^2 = \rho \cdot U_{21}^2 \quad (8)$$

With this equation all longitudinal elastic constants (Eq. 3-5) can be determined from longitudinal waves with the longitudinal group velocity, which is indexed as U_{kl} where $k = l = 1, 2, 3$. Index k is the direction of the cuboid sample and the identical direction in which the wave is emitted and detected is indexed with l .

All shear constants (Eq. 6-8) can be determined by using transversal waves (shear waves). Therefore, the transversal group velocity is indexed as U_{kl} where $k = 1, 2, 3$ is the direction of the cuboid sample in which the wave is emitted and detected and $l = 1, 2, 3 \neq k$ the direction in which the wave is oscillating (for Eq. 6, $k = 2$ and $l = 3$, for Eq. 7, $k = 1$ and $l = 3$, and for Eq. 8, $k = 1$ and $l = 2$), compare for example Mah et al. [36] or van Buskirk et al [37]. Due to the symmetry of the system, the values $kl = lk$ were summarized and averaged in the evaluation. To prove the isotropy of the material system, the system with the next lower symmetry was chosen and the stiffness matrix of an orthotropic material system is given (with all values different from zero) in the following equation 4:

$$C_{orthotropic} = \begin{bmatrix} C_{11} & C_{12} & C_{13} & & & \\ C_{12} & C_{22} & C_{23} & & & \\ C_{13} & C_{23} & C_{33} & & & \\ & & & C_{44} & & \\ & & & & C_{55} & \\ & & & & & C_{66} \end{bmatrix} \quad (9)$$

To complete, the the off-diagonal elements C_{12} , C_{13} and C_{23} must be defined. The equations for each are given in the following, [34,35,37]:

$$C_{12} = \sqrt{(C_{11} + C_{66} - 2\rho U_{12|12}^2)(C_{22} + C_{66} - 2\rho U_{12|12}^2)} - C_{66} \quad (10)$$

$$C_{13} = \sqrt{(C_{11} + C_{55} - 2\rho U_{13|13}^2)(C_{33} + C_{55} - 2\rho U_{13|13}^2)} - C_{55} \quad (11)$$

$$C_{23} = \sqrt{(C_{22} + C_{44} - 2\rho U_{23|23}^2)(C_{33} + C_{44} - 2\rho U_{23|23}^2)} - C_{44} \quad (12)$$

$U_{12|12}$ is the group velocity of a wave that is emitted and detected in a 45° angle between plane 1 and plane 2 of the sample. To obtain these off-diagonal elements, the sample cannot simply be a cuboid, but must have ground edges at an angle of 45° at the intersections of these planes, as it is given in Fig. 2.

Further details of the method can be found in other publications, as a representative summary is given by [37–41]. Latest publication of the method for the investigation of functionally graded materials was published by Nazeer et al. [42]. One of the authors of this work established in previous studies with other scientists this method for IMCCs (see Roy et al. [43–45]). In this study, the measurements were carried out using an electronic network analyzer of the type R3754A, Advantest, Tokyo, Japan. An evaluation software (within “LabView” by National Instrument, Austin, Texas, USA) written in previous work was used [40] on a connected computer, as well as two pairs of ultrasonic contact transducers (V122-RM, nominal central frequency 7.5 MHz and a diameter of the oscillator of 9.5 mm for longitudinal waves and V155-RM, nominal central frequency 5 MHz and an oscillator diameter of 12.7 mm for transversal waves, each of Olympus Deutschland GmbH, Hamburg, Germany). Commercially available food grade molasses was used as a couplant between transducer and specimen (molasses by Grafschafter Krautfabrik Josef Schmitz KG, Meckenheim, Germany). A thin, bubble-free film of the molasses was applied to the surface of the transducers and the sample was then clamped with the preload of springs between the transducers. The measurement was repeated three times and averaged, for each investigated orientation of the cube. As

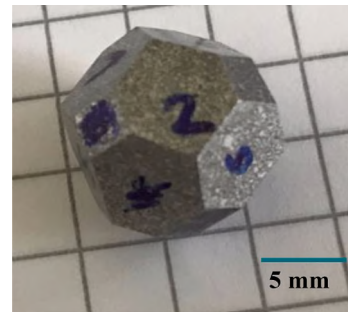


Fig. 2. Image of the prepared IMCC sample geometry (decaoctahedron) for measuring the coefficient of the stiffness matrix via UPS, with ground cube-edges in a 45° angle (hexagon) and original cuboid surfaces (squares).

referred above to the respective literature, the ratio of the longitudinal and transverse velocities is used to calculate the elastic modulus. The effective elastic modulus and the universal anisotropy index are calculated according to Soyarslan et al. [46] in several steps from the elastic tensor, shear and bulk moduli and Poisson ratio, using Voigt and Reuss assumptions, as well as the combination.

2.3. Resonant frequency damping analysis (RFDA)

RFDA, also referred to as impulse excitation technique (IET), was used as non-destructive characterization method to determine the elastic properties and the damping of the material. The RFDA has been used in previous publications and its suitability for determination of elastic properties at room and elevated temperatures has been investigated. Radovic et al. compared static and dynamic techniques for the determination of the elastic properties of different solids at room temperature. 4-point bending (4PB) and nanoindentation (NI), as well as impulse excitation technique (IET) and resonant ultra-sound spectroscopy (RUS) were used. The authors found that precision and repeatability of the dynamic methods (IET and RUS) are superior compared to the static methods (4PB and NI). Furthermore, the difference in results from IET and RUS are not statically significant [47]. The elastic properties at application temperatures are of particular interest for the design. Höning et al. investigated the suitability of the RFDA for the measurement of the elastic properties of a fiber reinforced ceramic matrix composite (CMC) at room and elevated temperatures. The elastic modulus determined via RFDA and 4PB showed comparable results at RT. The dynamic elastic modulus of the CMC has been successfully measured up to 1250°C using the RFDA and agrees well with the modeling results using FEM [48].

The AlSi10Mg and IMCC samples were heat treated at 500°C with a heating rate of 5 K/min, holding time of 10 minutes and cooling without temperature control < 5 K/min in a LVT 9/11 ashing furnace (Nabertherm GmbH, Lilienthal, Germany) under atmospheric air prior to RFDA testing to minimize the influence of residual stress from manufacturing.

The fundamental flexural and torsional resonant frequencies were measured at room and high temperature using a RFDA Professional and RFDA HT1600 setup (IMCE NV, Genk, Belgium). The frequencies were used to calculate the elastic properties like the elastic modulus, shear modulus and Poisson's ratio.

The elastic E and shear modulus G can be calculated from the sample mass m , length L , width b , thickness t and the fundamental flexural f_f and torsional f_t frequencies. The correction factors T_1 and R were calculated according to ASTM E1876-15 [49].

$$E = 0.9465 \left(\frac{mf_f^2}{b} \right) \left(\frac{L^3}{t^3} \right) T_1 \quad (13)$$

$$G = \frac{4Lmf_t^2}{bt} R \quad (14)$$

For an isotropic material, the Poisson's ratio ν can be obtained from the elastic and shear modulus by eq. (15).

$$\nu = \frac{E}{2G} - 1 \quad (15)$$

Room temperature (RT) measurements were carried out using a 3 mm metal projectile with a node distance of 30 mm and an impulse power of 50 %. For the high temperature (HT) measurements a 3 mm Al2O3 projectile, a node distance of 33 mm and an impulse power of 50 % were used. To determine the flexural and torsional frequencies simultaneously, the automatic excitation unit and the microphone were positioned at diagonally opposite corners for the RT and HT measurements. For the HT experiment individual measurements were performed every 5 K in heating- and cooling phase and for selected samples additionally every 60 s during the dwell time (see Fig. 3,a). The thermal expansion of the samples in the HT measurements were not considered in the calculation due to the small difference between the corrected and uncorrected graph of the elastic modulus with <0.5 GPa between all individual measurement points.

Quenching experiments of the IMCC sample were carried out in a furnace (LT 5/13, Nabertherm, Lilienthal, Germany) at 500°C with a heating rate of 5 K/min and a dwell time of 60 min under atmospheric air (see Fig. 3,b). After heat treatment, the specimen was removed from the furnace and immediately quenched with air (compressed air pistol, 8 bar) or in silicone oil Fragoltherm X-400-A, by FRAGOL AG, Mülheim, Germany at room temperature.

2.4. Dilatometry

For determination of the coefficient of thermal expansion over the temperature, dilatometry measurements were carried out in a DIL 402 Expendis Select, horizontal push-rod dilatometer from NETZSCH-Gerätebau GmbH, Selb, Germany. The resolution of the length is accurate to 1 nm and the temperature is accurate to 1 K. The data acquisition rate was set to 75/min. To determine the CTE, a local derivative was calculated between each data point. The temperature profile was chosen to be 0... T_{max}...25°C. Maximum temperature (T_{max}) was set to 260, 285, 310, 335, 360 and 500°C, in accordance with the RFDA measurements for the region of interest. T_{max} = 500°C was chosen for

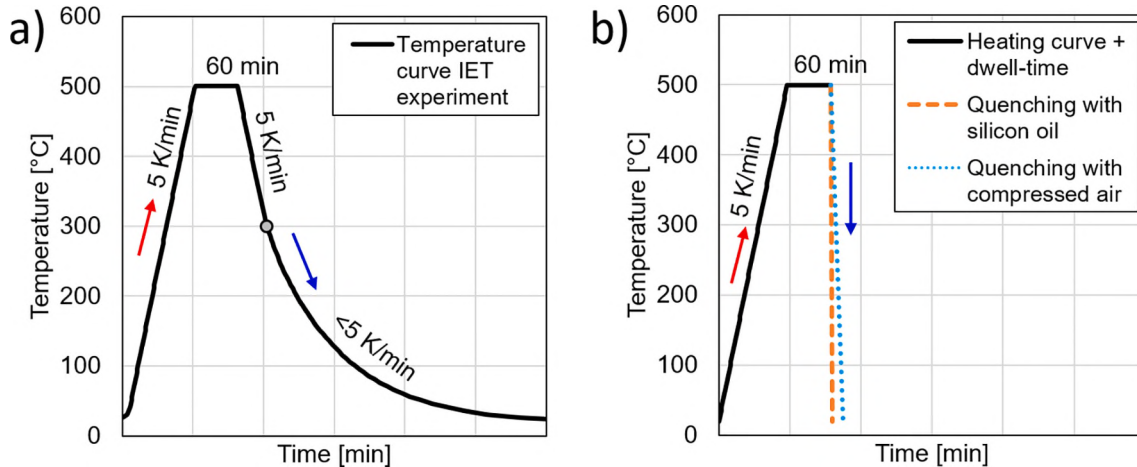


Fig. 3. a) Temperature profile of an IET HT experiment with heating phase, dwell time and cooling phase. b) Scheme of the temperature profile of the quenching experiment; the cooling rate during quenching was not determined. Arrows indicate the heating (red) and cooling (blue) curves.

comparison with literature values. For each T_{\max} , two samples were measured for three cycles of which the latter two were evaluated. Measurements were carried out by starting with the lowest T_{\max} . As described by Huber et al. [50], the heat treatment during production has a significant impact on the heating curve of the first measurement resulting in a peak. From the second measurement onwards, the curves are reproducible. Therefore, the first measurement was excluded, and the data shown start from the second cycle on. The sample were measured from lowest to highest T_{\max} . The heating and cooling rate was 5 K/min and the holding time at T_{\max} was ten minutes. For temperatures lower than 75°C, the values were neglected as the heating rate was process-related not constant (see Fig. 7,b). Other authors describe this for temperatures below 100°C, as they observed minor fluctuations [11]. The pre-load was set to 0.2 N and the furnace was rinsed with a nitrogen gas flow of 20 ml/min. The furnace had been calibrated beforehand at these parameters with the second measurement of a cylindrical calibration body (NETZSCH-Gerätebau GmbH, Selb, Germany, order number: 6.219.1-92.2) made of polycrystalline solid aluminum oxide material. It had a length of 25 mm and a diameter of 6 mm. The measurement was carried out in accordance with DIN 51045:20 05-08 [51]. The highest 35 K were cut away uniformly, as the cooling rate had to set in. The data was postprocessed with a 13-fold smoothing in the NETSCH Proteus software to remove measuring related artifacts.

3. Results

3.1. Ultrasonic phase spectroscopy

The elastic constants as well as the elastic modulus were calculated from UPS measurements for the ceramic foam, the AlSi10Mg alloy and the IMCC, as described in chapter 2.2. Results of the stiffness matrix, elastic modulus, Poisson's ratio, and the universal anisotropy index A_u are presented in Table 1. Here, for each material, four samples were prepared and measured. The standard deviation between the measurements was calculated according to Cohen [52]. For the preform it ranges between 0.3 % and 1 %. The deviation for the alloy lies between 0.5 % and 1.6 %. The largest standard deviation is found for the IMCC ranging from 0.3 % to 2.4 %.

3.2. Resonant frequency damping analysis

Results of the room temperature measurements of the IMCC, AlSi10Mg and ceramic foam samples are summarized in table 2. Investigated samples have dimensions of ca. $60 \times 10 \times 4 \text{ mm}^3$ except an additional sample IMCC-2 with dimensions of ca. $57 \times 8 \times 1.6 \text{ mm}^3$. The elastic properties of both IMCC samples are similar in terms of elastic and shear modulus as well as Poisson's ratio. The difference in the flexural and torsional frequencies are due to the different sample dimensions. The standard deviation of the calculated elastic properties, especially the elastic modulus, is relatively high. As the accuracy of the calculated elastic modulus mainly depends on the precision of the specimen thickness (see Eq. 13). It could be further reduced by a more accurate fabrication of the specimens e.g., an improved grinding process. However, the standard deviation refers to the absolute value of the E- and G-modulus. In comparative RFDA measurements of the same

Table 2

Elastic properties of the IMCC, AlSi10Mg and Al2O3 foam samples measured with the RFDA at room temperature.

Sample	Flexural Frequency [Hz]	Torsional Frequency [Hz]	E-Modulus [GPa]	G-Modulus [GPa]	Poisson's ratio
IMCC-1	7293	24719	109.0 ± 5.5	42.7 ± 0.9	0.276
IMCC-2	3040	12198	110.7 ± 3.9	43.2 ± 0.6	0.281
AlSi10Mg	5314	17266	78.9 ± 4.2	29.8 ± 0.7	0.324
Al2O3 foam	3445	10938	12.3 ± 1.9	4.7 ± 0.3	0.309

sample, changes that are smaller than the standard deviation can also be considered.

The IMCC and its components AlSi10Mg and Al2O3 foam were measured up to 500°C with a rate of 5 K/min and a dwell time of 10 min. The elastic modulus versus temperature graph is shown in Fig. 4,a. Each point of the graph represents an individual measurement of the heating- and cooling phase of the experiment. The ceramic foam shows a relatively low elastic modulus of 12.0 GPa at 20°C, which decreases slightly to 11.0 GPa at 500°C. The AlSi10Mg sample yields an elastic modulus of 77.7 GPa at 20°C, which decreases with increasing temperature. At 500°C the elastic modulus is 51.6 GPa, which means a reduction of about 34 %. The elastic modulus of the IMCC with a value of 112.7 GPa is significantly higher compared to its individual components. At 500°C the elastic modulus decreases by 27 % to 82.4 GPa. After reaching the maximum test temperature and during the dwell time the elastic modulus of the IMCC increases by 4.1 GPa, which leads to a gap (hysteresis) between the heating and cooling curve. This hysteresis closes at around 100°C. It is worth noting, that the elastic moduli before and after the HT experiment show comparable values (± 1 GPa) for the IMCC and its individual components. Therefore, it is assumed that during a single heating and cooling cycle no significant irreversible changes occurred in the materials.

In Fig. 4,b the elastic modulus versus temperature is shown for IMCC samples which were tested up to 500°C and different dwell times of 10 and 60 minutes. A minimum offset in elastic modulus of 1 GPa at 20°C is recognizable and remains almost constant during the entire experiment. Overall, the reproducibility of the HT measurement is quite good. Both graphs show the same curve progression. The increase of the elastic modulus at maximum test temperature and during the dwell time differs slightly for the investigated samples. The elastic modulus increased by 4.1 GPa for 10 minutes dwell time and by 5.6 GPa for 60 minutes dwell time. After the HT cycle the elastic modulus is comparable to the initial value but shows a slight reduction (< 0.6 GPa).

Fig. 5 shows cyclic measurement for the IMCC up to different maximal temperatures, holding for a dwell time of 10 minutes. The heating- and cooling rate was set to 5 K/min. However, the cooling power was limited, which led to a lower cooling rate of < 5 K/min for temperatures $< 300^\circ\text{C}$ (see Fig. 5,b). All measured samples show a decrease of the elastic modulus with increasing temperature (Fig. 5,a). The progression of the heating and cooling curve of the IMCC 260°C

Table 1

Determined stiffness coefficients (with standard deviation of the material), elastic moduli and Poisson's ratios and anisotropy indices of the Preform, the metal and the IMCC. All values are given in GPa (except for ν and A_u which have no unit).

Material	C_{11}	C_{22}	C_{33}	C_{44}	C_{55}	C_{66}	C_{12}	C_{13}	C_{23}	E_{11}	E_{22}	E_{33}	E_{eff}	ν	A_u
Al ₂ O ₃ -Preform	27.4 ± 7.1	29.0 ± 1.84	29.9 ± 2.80	9.1 ± 1.67	8.7 ± 0.19	8.6 ± 0.78	8.9 ± 1.65	8.4 ± 3.62	9.1 ± 8.33	20.7 ± 2.23	24.3 ± 0.35	22.4 ± 1.32	20.6 ± 1.71	0.27 ± 0.02	0.23 ± 0.18
AlSi10Mg	113.5 ± 0.36	113.3 ± 4.91	113.3 ± 1.06	29.7 ± 1.22	28.7 ± 0.40	29.3 ± 1.29	52.4 ± 2.32	54.7 ± 0.73	49.3 ± 0.96	76.6 ± 0.22	76.4 ± 0.67	76.8 ± 0.89	78.2 ± 1.49	0.32 ± 0.004	0.01 ± 0.003
IMCC	146.9 ± 2.44	144.2 ± 3.12	140.9 ± 6.15	42.8 ± 2.66	43.3 ± 2.33	42.6 ± 1.48	77.2 ± 7.12	72.7 ± 9.48	73.6 ± 2.66	110.9 ± 4.76	110.2 ± 4.99	110.2 ± 6.20	103.9 ± 5.23	0.32 ± 0.01	0.09 ± 0.06

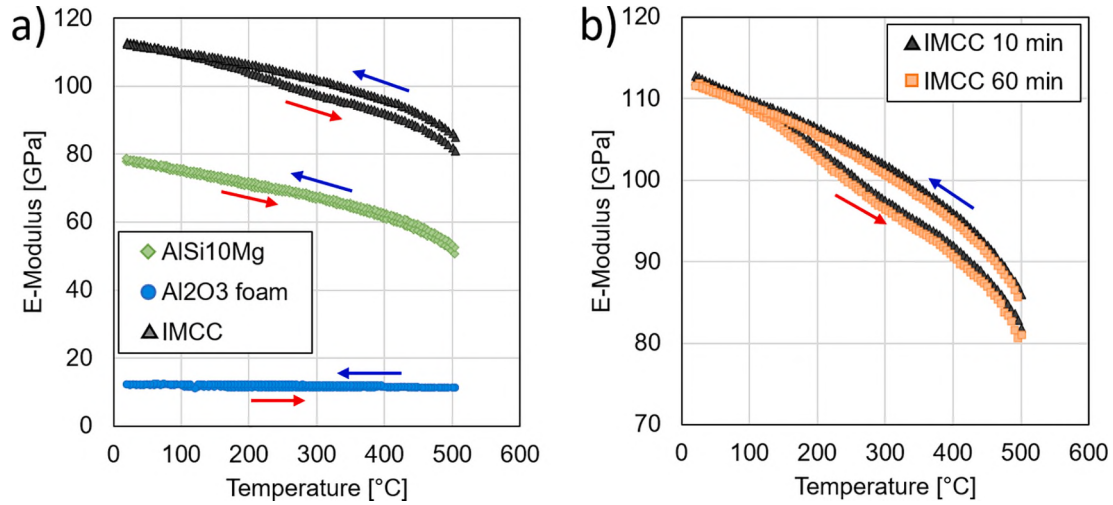


Fig. 4. Elastic modulus versus temperature in the range from RT to 500°C using the RFDA. a) Comparison of the IMCC and its components with a dwell time of 10 minutes. b) Comparison of the IMCC measured at different dwell times of 10 and 60 minutes. Arrows indicate the heating (red) and cooling (blue) curves.

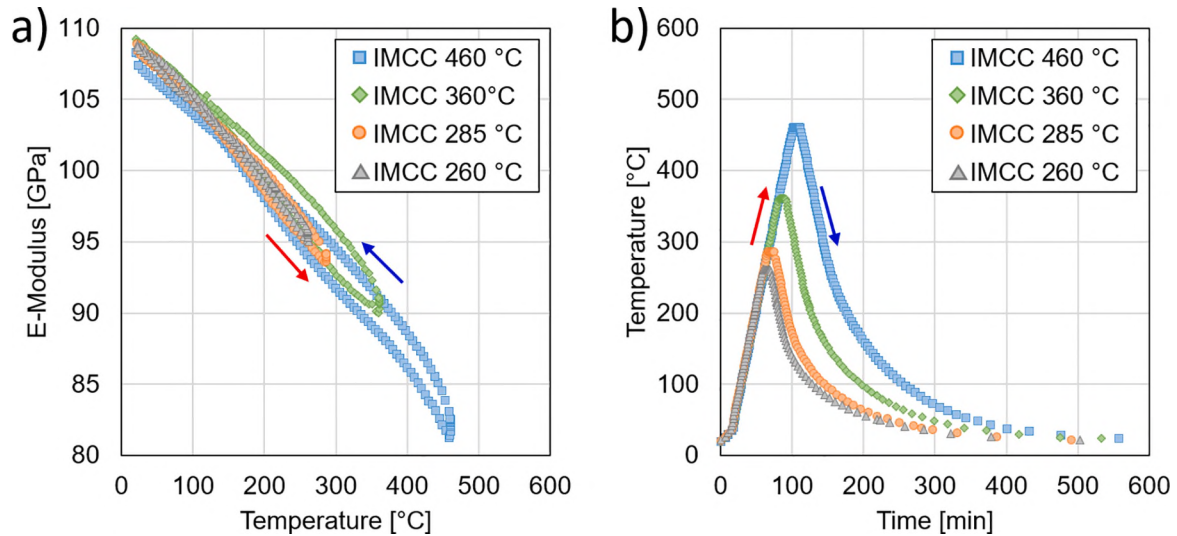


Fig. 5. a) Comparison of the IMCC elastic modulus measured in different temperature ranges with a dwell time of 10 minutes using the RFDA. b) Corresponding temperature curves. Arrows indicate the heating (red) and cooling (blue) curves.

sample is nearly the same. Starting with the IMCC 285°C sample, a small hysteresis effect can be observed. The elastic modulus increases slightly after reaching T_{max} . Samples IMCC 360°C and IMCC 460°C also show the hysteresis effect in a more pronounced form. After the 10 min dwell time, the elastic modulus increases further with decreasing test temperature for all samples. In the range of 100 to 140°C, the cooling curves crosses the heating curves. From then on, the elastic modulus of the cooling curve shows lower values than during heating. The elastic modulus at the beginning and the end of the high temperature experiment is comparable but tends to show a slight decrease <1 GPa. As mentioned above, the HT experiments are comparative measurements of the same specimen, therefore also smaller differences in the elastic constants (smaller than the standard deviation) can be considered.

The results of the quenching experiments (described in chapter 2.3) are presented in table 3. The elastic properties of the IMCC were measured with the RFDA at RT before (-1) and after (-2) the quenching with compressed air (IMCC-Air) or silicone oil (IMCC-Oil). The idea of the quenching test was to check, if the increase in elastic modulus observed at 500°C and a dwell time of 60 min (see Fig. 4,b) by quenching, leads to a permanent change in the elastic modulus at RT.

Table 3

Elastic properties of the IMCC sample measured with the RFDA at RT before (-1) and after (-2) quenching experiment with compressed air or silicone oil.

Sample	Flexural Frequency [Hz]	Torsional Frequency [Hz]	E-Modulus [GPa]	G-Modulus [GPa]	Poisson's ratio
IMCC-Air-1	7379	25008	111.6 ± 6.0	43.7 ± 0.9	0.277
IMCC-Air-2	7340	24875	110.4 ± 6.0	43.3 ± 0.9	0.275
Difference	39	133	1.2	0.4	
IMCC-Oil-1	7348	24898	110.6 ± 6.0	43.3 ± 0.9	0.277
IMCC-Oil-2	7298	24748	109.1 ± 6.0	42.8 ± 0.9	0.275
Difference	50	150	1.5	0.5	

The expectation of freezing the state that exists at high temperature, which would result in a higher elastic modulus at RT, is not met. Quenching with compressed air revealed a slight reduction by 1.2 GPa in elastic modulus and by 0.4 GPa in shear modulus. The IMCC-Oil sample

shows a comparable reduction in elastic modulus by 1.5 GPa and shear modulus by 0.5 GPa.

3.3. Dilatometry

As previous results have shown in literature, dilatometry experiments at single interpenetrating composites and their components were investigated. To focus on the ongoing phenomena during heating and cooling, the development of the curve with increasing maximum temperature (T_{max}) in comparison to the RFDA results is the key point of the investigation. Nevertheless, the microstructure and processing technique of the here investigated ceramic preform and IMCC is unique, and the used metal alloy differs from other investigations, where pure aluminum [11,28] or Al12Si [29] was used. Therefore, a comparison of the dilatometry results for the IMCC and its components is given in Fig. 6.

When comparing the ceramic preform, the AlSi10Mg alloy and the IMCC, the ceramic foam has the lowest CTE of about $6.3 \cdot 10^{-6}$ 1/K, slightly increasing over the whole range of tested temperatures up to $8.5 \cdot 10^{-6}$ 1/K. The metallic CTE ranges from 2.17 to $2.67 \cdot 10^{-5}$ 1/K and decreases from ca. 350°C on down to $2.39 \cdot 10^{-5}$ 1/K. The IMCCs CTE increases up to 240°C from 1.4 to $1.8 \cdot 10^{-5}$ 1/K and decreases down to $7.3 \cdot 10^{-6}$ 1/K, for temperatures above 450°C. At this temperature, the CTE of the IMCC falls below the CTE of the ceramic preform, which will be discussed below. Cooling curves for the ceramic preform are identical to the heating curves. For the AlSi10Mg alloy, the curve also shows good agreement between heating and cooling, as the standard deviation of heating and cooling overlap up to temperatures above 420°C. The cooling curve of the IMCC differs strongly from the heating curve. For cooling, the CTE increases above $1.7 \cdot 10^{-5}$ 1/K first, decreases to a local minimum of $1.3 \cdot 10^{-5}$ 1/K at 310°C, increases again up to $1.6 \cdot 10^{-5}$ 1/K in a local maximum and finally reaches values close to $1.2 \cdot 10^{-5}$ 1/K below 100°C.

For the closer understanding of the phenomena of the composite and the difference in heating and cooling curve for CTE for different temperatures, the resulting CTE curves for different maximum temperatures are shown in Fig. 7. Heating curves for each T_{max} and each sample are shown in warm colors (red and brown), cooling in cold colors (blue and purple). As it can be seen in the figure, heating and cooling align well for low T_{max} . With increasing maximum temperature, they begin to differ. For $T_{max} > 310^\circ\text{C}$ the heating curve cuts across the cooling curve at high temperatures. The phenomenon becomes extreme for higher T_{max} and

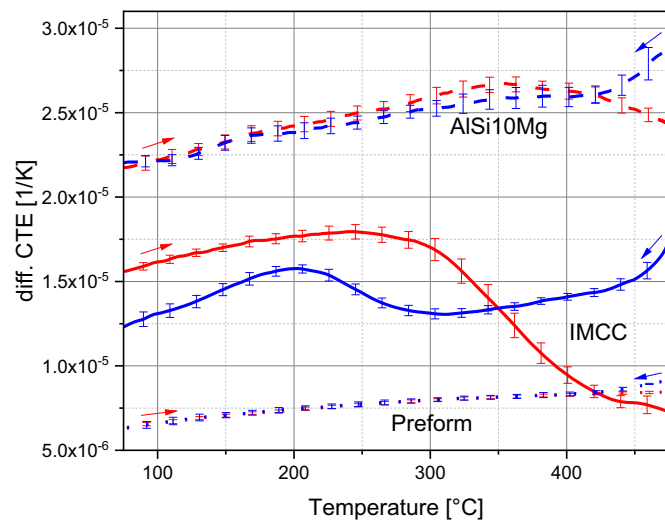


Fig. 6. Overview of the averaged CTEs for the ceramic preform, the AlSi10Mg alloy and the IMCC of each 3 samples in the range of 0...500...25°C. Heating is colored in red and cooling in blue.

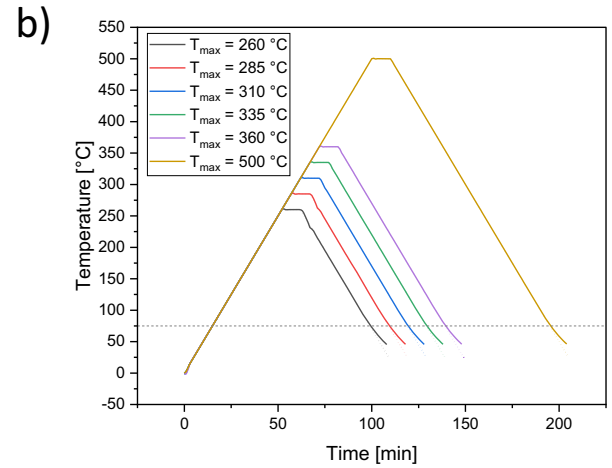
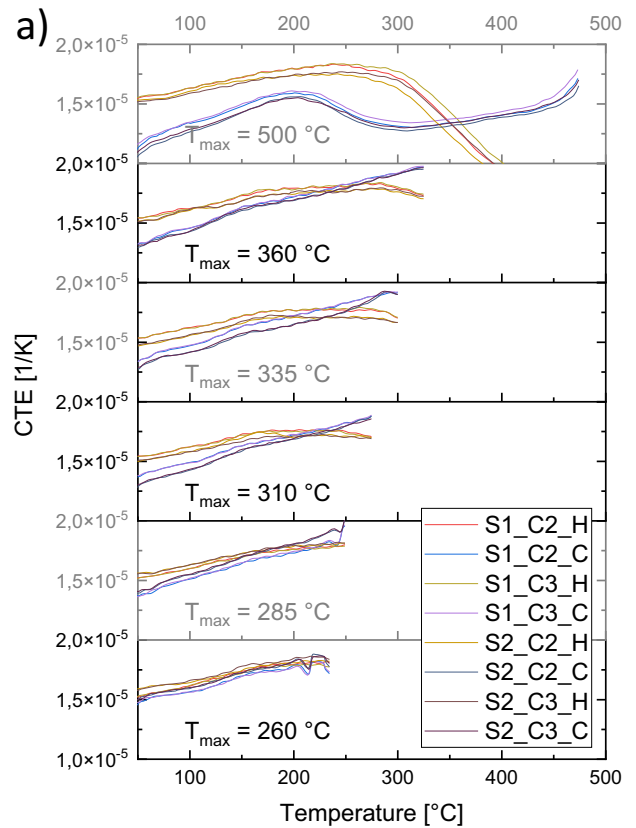


Fig. 7. a) Overview of the CTEs of samples S1 and S2 for different T_{max} . C2 and C3 indicate cycle 2 and 3, a heating phase is indicated with H and warm colors, cooling with C and cold colors. Areas with non-constant heating or cooling rate are removed from the graph. b) Overview of the temperature over time diagram for each T_{max} with given target curve (dotted line) and the measured curve (continuous line).

the cooling curve starts to change its behavior, as it can be seen between the cooling curve of $T_{max} = 360$ and $T_{max} = 500^\circ\text{C}$.

4. Discussion

4.1. Determination of elastic constants

For room temperature, the elastic modulus measurements show very good agreement between ultrasonic phase spectroscopy and resonant frequency damping analysis for the IMCC and the AlSi10Mg alloy. Also, the low anisotropy index shows that almost perfect isotropy (anisotropy index = 0) is detected. In comparison to previous studies with smaller

samples and slightly differing processing parameters, the values show small difference in the range of less than 5 % [30]. The values of the ceramic preform differ in a higher range. The scattering of the stiffness and elastic modulus in between the samples brings up the big anisotropy index. A deviation is visible in the numerical modelling of the elastic modulus in comparison to the measured values via UPS in Horny et al. [30]. The difference between the methods UPS and RFDA lay in the same range. Reasons can be found in the high damping property of the highly open porous ceramic foam, which leads to resonance and high absorption and therefore to a strongly noisy signal, which makes evaluation difficult. Due to the frequency sweep carried out in the UPS method, these resonant frequencies can be compensated in a certain range, nevertheless, the determination of the slope was difficult for the ceramic foam. Next to this, local differences in the microstructure, invisible pre-damage in the samples during the preparation and transport can be further reason for minor difference. The very high isotropy of the IMCC also underlines the high isotropy of the ceramic foam, as the signal in the composite is way easier to measure, and no significant anisotropic influence arose through the ceramic preform (compare Roy et al. for the influence of the preform on the elastic anisotropy in their composite [29]). As the comparison to the data sheet (cf. [53,54]) shows, usually a range of elastic modulus of about 5 - 10 % is observed, which shows, that the exact determination of the elastic properties, even in an industrial and reproducible process, shows deviations in the range of the here measured material. Therefore, the frequency based approach with UPS and RFDA show both reproducible and precise results, compared with other determination methods for elastic constants (cf. [47,55]).

4.2. RFDA

In the HT measurements the metal and ceramic foam do not show a significant difference between the heating and cooling curve (hysteresis). Therefore, the individual components of the IMCC (AlSi10Mg and ceramic foam) are not considered for the hysteresis phenomena. A hysteresis is only observed for the IMCC. After reaching the dwell time at maximal test temperature the elastic modulus of the IMCC starts to increase. This strengthening effect is observed for test temperatures of 285, 360, 460 and 500°C, except 260°C (Fig. 5,a) and is more pronounced for higher test temperatures (360, 460 and 500°C). A significant dependence on the dwell time at 500°C is not found (see Fig. 4,b). However, further experiments are required to prove if a longer dwell time at test temperatures of 285 or 360°C would lead to a stronger hysteresis effect. Beside the increase in elastic modulus during the dwell time, we assume an additional increase or decrease in elastic modulus during heating or cooling, respectively. However, these effects are barely visible in the measurement curves due to the superposition with the temperature-dependent increase or decrease of the elastic modulus. Therefore, the effect is explained schematically in Fig. 8. The total heating and cooling curve of the elastic measurement (E_{total}) can be split into a thermal part ($E_{thermal}$), based on the physical expansion of homogeneous materials, and a hysteresis part ($E_{hysteresis}$), which becomes evident from the difference between the total elastic curve and the

thermal weakening with increasing temperature.

Two possible explanations for the hysteresis behavior are given by Skirl [11]. According to the first explanation pores are formed during cooling by exceeding the cavitation stress. These pores close again during heating due to the expansion of the metal. The pores result in a volume difference, which in turn causes stress and thus the hysteresis. Balch et al. [28] also attributed the hysteresis behavior of the coefficient of thermal expansion (CTE) to the presence of micro voids at the metal/ceramic interface. Skirls second explanation describes that during heating and cooling, an intrusion/extrusion process takes place, in which the metallic phase flows to the surface and back into the sample through channels. This process requires tensile stress during cooling and compressive stress during heating in the metal phase. The hysteresis is induced by the reversal of the stress. Also, a combination of both processes is possible (cf. Skirl et al. [11] and Hoffman et al. [20]). The second explanation by Skirl might not be so relevant for the here investigated IMCC, due to the residual porosity and a significant difference in the metal/ceramic content of the composite (metal content of Skirl 13-40 % versus 74 % in the IMCC). In addition, the very fine-pored ceramic foam used here creates a kind of throttling effect, which is why very high pressures would presumably be required for plastic flow of the metal phase. By comparison, 60 bar is already required for complete infiltration of the ceramic preform at a significantly higher temperature of 700°C, with the molten metal phase. Castillo-Hernandez et al. investigated Mg2Si, Mg2Sn and their solid solutions in RFDA HT measurements and also found a hysteresis for the elastic modulus. The authors attributed the hysteresis behavior to a microcrack healing process that occurs at HT and a re-opening of the cracks in the cooling phase due to thermal stress [55].

Repeated measurements of the IMCC at HT revealed a decrease of the elastic modulus at RT. Roy et al. attribute the lower elastic modulus to a decrease of internal stress in the composite due to the HT treatment [29]. Another point of view might be, that the lower elastic modulus indicates an increasing damage (defect accumulation) of the specimen by thermal cycling. This assumption is consistent with the description by Delannay, that thermal cycling in metallic composites can lead to deformation or degradation of the composite properties as a result of damage accumulation [27]. Further experiments are required to clarify these observations. However, this publication focuses on the explanation of the hysteresis behavior, therefore no further experiments regarding a possible damage due to thermal cycling and the underlying damage mechanism were performed at this point.

The quenching experiments with compressed air and silicone oil did not result in a higher elastic modulus at room temperature. The condition at HT with the increased elastic modulus (hysteresis) cannot be kept frozen with the applied methods. Instead, the quenching resulted in a small decrease in elastic modulus at room temperature. It can be assumed that the rapid cooling due to the highly different CTE's resulted in internal stress probably causing microcracks in the composite structure. This is more in line with Delannay since the above-mentioned reduction of internal stress due to quenching is unlikely.

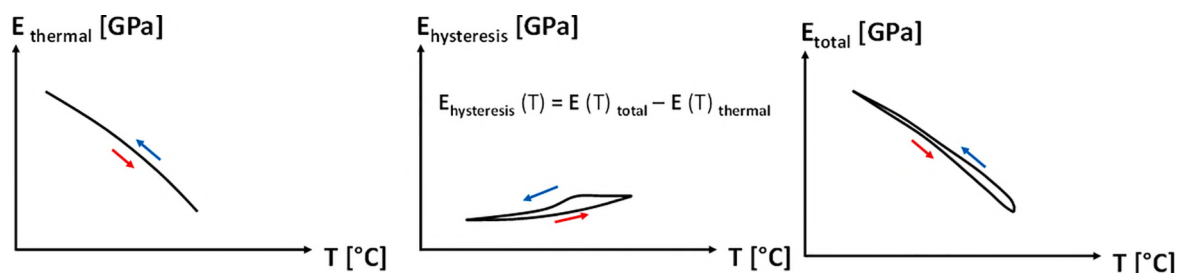


Fig. 8. Schematic behavior of the elastic modulus E over the temperature T , from temperature dependency (left), hysteresis part (center) and the resulting curve (right).

4.3. Dilatometry

In comparison to literature, the curve of the alloy differs from the results of Jiang, et al. [56], as they measure CTEs for the AlSi10Mg alloy between 1.3 and $3.7 \cdot 10^{-5}$ 1/K, with a strong slope up to 250°C and decrease to $3.5 \cdot 10^{-5}$ 1/K at 350°C . Better agreement of the data is found with Gumbleton et al. [57] for their measured range up to 450 K (ca. 175°C). This is confirmed in the data sheet, where a range of 2 to $2.4 \cdot 10^{-5}$ 1/K is given (e.g. [53]) and justifies the correct and precise measurement, regarding DIN 51045:20 05-08 [51].

The CTE of the composite at RT is around $1.4 \cdot 10^{-5}$ 1/K. In comparison to the rule of mixture, calculated from the ceramic foam and the alloy, a value of $1.8 \cdot 10^{-5}$ 1/K should be reached. When comparing the experimental value with the rule of mixture of the metallic alloy and an alumina bulk material [53], the tested IMCC still shows a lower value. Explanation can be found in the interpenetrating structure, as the expansion of the metallic phase is restricted by the ceramic. Next to this, the internal tensile stress in the metallic phase, as described by Delannay [27], can also reduce the expansion of the aluminum alloy. As the inner stress in the metallic phase decreases with increasing temperature, the limited expansion is reduced and the CTE is increasing. It reaches a maximum at ca. 240°C , before it starts to decrease. At this temperature, 0.6 times of the absolute melting temperature is exceeded (237°C for 577°C of the melting temperature of the eutectic composition) and thermal activated self-diffusion in the metallic phase becomes dominant [58]. The declining slope in the curve below this temperature can be explained by the fact that (internal) stress reduces the creep onset locally [59] (stress over E-module vs temperature over melting temperature diagram).

Compared with the stepwise increased T_{\max} (see Fig. 7), the phenomena of a revealing hysteresis between heating and cooling sets in between 260 and 285°C , where the CTE reaches a plateau around the maximum. For elevated temperatures, but clearly higher temperatures than the IMCC (ca. 350°C), the CTE of the AlSi10Mg alloy also reaches a plateau and starts to decrease. The earlier decrease in the CTE for the IMCC can be explained by the above-mentioned inner stress in the metallic phase, built up during manufacturing from liquid metal phase and reversed in each cooling cycle, as the interpenetrating ceramic phase surrounds the metallic phase. For temperatures above 360°C , the heating and cooling curves not only split up, but the cooling behavior shows a significant change. Furthermore, a hysteresis is revealed in the CTE curve, caused by creep, as it can be seen in Fig. 7.

On microstructural level, but below the resolution of visibility (compare Prielipp et al. [60], who carried out TEM investigation, but could not see the expected occurring porosity of 0.5 to 2.9% , as stated in Skirl et al. [11]), the decrease of microporosity by expansion of the metallic phase into the voids decreases the thermal expansion [28]. As Balch et al. stated, from a very small porosity content on or even by interfacial debonding, the CTE is lowered in an IMCC. Both, interfacial detachments and residual porosity could be found in the IMCC, as previous studies have shown [30,31,33]. Close to 400°C , the metallic phase lost its strength by further softening and the ceramic phase clearly dominates the CTE in the composite. The finally reached value (below the CTE of the ceramic preform) can be explained by the transverse strain inhibition of the metallic phase for the ceramic struts. This leads, in comparison to the empty pores in the ceramic foam, to a further restriction in expansion. The CTE of the composite reaches values of dense alumina bulks, in the range of $7 \cdot 10^{-6}$ 1/K [53].

For cooling, contrary effects to those during heating take place. The softened metallic phase, fully bond to the ceramic with closed interfacial detachment, builds up inner tensile stress and increases the CTE during cooling. Depending on the chosen T_{\max} , values at a maximum of $2 \cdot 10^{-5}$ 1/K are reached, lying far above the heating curve. Reversal interfacial detachment and increasing microporosity stepwise decrease the sudden increased CTE of the cooling curve. The higher T_{\max} , the higher values are reached by the CTE, as the difference in the phenomena of inner

stress and occurring porosity increases. At about 200°C , the heating and cooling curve cross each other for T_{\max} up to 360°C . Below this, the CTE of the cooling is below the one of the heating curve. For $T_{\max} = 500^\circ\text{C}$, the cooling curve lies below the heating curve from 350°C on, but has a local maximum at 200°C . The value of the maximum is equal with the room temperature CTE of the heating curve. A clear explanation for this phenomenon could not be found yet.

Due to the interpenetrating structure of the composite, it has to be assumed, that inner material damage occurs over the cycles, as the inner stress would lead to hydrostatic stress and cannot be compensated by the aluminum phases alone (compare Skirl et al. [11] with their theory of intrusion/extrusion of aluminum). As plastic deformation can only take place in the metallic phase, damage in the ceramic phase is expected for a higher number of cycles.

4.4. Influence of the processes in the material on the thermal expansion coefficient and the elastic properties at elevated temperature

As discussed in chapter 4.2 and 4.3, a temperature dependent correlation of both, the elastic properties and the thermal expansion coefficient could be investigated for interpenetrating metal ceramic composites. The hysteresis behavior occurs above a certain temperature. For the investigated IMCC this temperature lies between 260 and 285°C . This is relevant for component dimensioning and use in elevated temperature environments, where a change in the behavior must be considered.

As the discussion of the results and comparison to literature shows, the complex microstructure and the interaction of the phases plays a key role for the investigated phenomena. Residual stress in the material, their decrease in the metal phase with increasing temperature, the onset of creep and plasticity associated with changes in porosity, interface detachment and defects influence the investigated properties.

Roy et al. [29] stated for the investigation of anisotropic interpenetrating phase composites, that there is a correlation between the elastic modulus and the thermal expansion. With a look at the examinations made, we can extend this correlation, as the investigations show a direct connection of the effects, occurring in the elastic properties under elevated temperatures and in the thermal expansion experiments in general.

Studies on the internal stress in IMCCs have already proven the complex interaction inside the interpenetrating composite and the load-transfer at room temperature under load (cf. [21,23]). As this study shows (in comparison to studies with higher ceramic contents [11,20,28]), the material combination and phase ratio influences the thermal expansion, the domination of the two phases and different mechanisms. For high temperatures (well above 0.6 times of the absolute liquidus temperature of the metallic phase) the ceramic phase dominates the composite and restricts the thermal expansion.

Skirl et al. [11] stated the dominance of the ceramic phase for the thermal behavior of the composite for high ceramic contents above 75 vol.-%. For lower ceramic contents the major influence in both investigated hysteresis phenomena has to be attributed to the metal phase and the interaction at the interface, next to porosity and initial defects in the material.

5. Conclusion

Different conclusions can be made regarding the thermal expansion behavior and the elastic properties at elevated temperatures:

- A hysteresis effect occurs for the investigated IMCC above 260°C in thermal expansion as well as in the elastic properties. By experimental investigation a schematic description of the phenomena could be derived, differentiating between a thermal and a hysteresis component. The hysteresis component includes porosity, surface

detachment and defect effects, as well as softening of the metal phase by creep, plasticity and changes of the internal stress distribution.

- Unexpected at first sight, the increasing CTE of the IMCC drops from above 300°C strongly to a minimum value of $7 \cdot 10^{-6}$ 1/K, below the ceramic foam. Closer comparison showed, the CTE of the IMCC drops to the value of the ceramic bulk material and microstructural explanations are elaborated
- The cooling curve of the CTE changes its behavior strongly for 360°C $< T_{\max} < 500^\circ\text{C}$, due to the above-mentioned effects within the metallic phase.
- The elastic modulus increases for the cooling curve above 260°C, but is – within the framework of the findings made – not dependent on dwell time at the maximum temperature.
- The properties of the changed elastic modulus at high temperatures cannot be conserved to room temperature by quenching the sample, as the elastic modulus always returns to its initial value.

6. Outlook

In the RFDA experiments a temperature dependence of the hysteresis behavior was found for the IMCC. A significant time dependence of the hysteresis for the tests at 500°C was not found. Further experiments need to be carried out to investigate, if a longer dwell time at lower temperature would lead to a stronger hysteresis, which would point to a diffusion-controlled process.

Further investigation needs to be done with regard to a possible damage accumulation in the IMCC which might occur due to thermal cycling or the quenching experiments. This might also contribute to the hysteresis component and needs detailed examination. The change in cooling curve behavior of the CTE between 360 and 500°C could be narrowed down by further experiments at temperatures in between. These could also help to explain the phenomena in the CTE cooling curve with $T_{\max} = 500^\circ\text{C}$ occurring around 200°C.

Funding

The financial support for this work in the context of the DFG research WE 4273/17-1 is gratefully acknowledged.

Data Availability Statement

The raw/processed data required to reproduce these findings cannot be shared at this time as the data also form part of an ongoing study.

Author statement

All authors have seen and approved the final version of the manuscript. The article is the author's original work and has not received prior publication and is not under consideration for publication elsewhere.

CRedit authorship contribution statement

Joél Schukraft: Conceptualization, Investigation, Writing – original draft. **Jan Roßdeutscher:** Investigation, Writing – original draft. **Frederik Siegmund:** Investigation, Writing – original draft. **Kay A. Weidenmann:** Writing – review & editing.

Declaration of Competing Interest

The authors declare that they have no known competing financial interests or personal relationships that could have appeared to influence the work reported in this paper.

Acknowledgments

The authors would like to thank P. Mechnich and M. Welter (DLR Institute of Materials Research) for helpful discussion and proofreading. The friendly supply of complimentary preform material by Morgan Advanced Materials Haldenwanger GmbH is gratefully acknowledged.

References

- [1] B.O. Malomo, O.T. Ogunbodede, O.T. Popoola, K.M. Oluwasegun, S.A. Ibitoye, L. O. Adekoya, A Design Optimization of the High Pressure Die Casting Process for the Fabrication of Bulk Metal Matrix Composites, *Matls. Perf. Charact.* 6 (2017), 20170052, <https://doi.org/10.1520/MPC20170052>.
- [2] F. Scherm, R. Völkl, A. Neubrand, F. Bosbach, U. Glatzel, Mechanical characterisation of interpenetrating network metal–ceramic composites, *Materials Science and Engineering: A* 527 (2010) 1260–1265, <https://doi.org/10.1016/j.msea.2009.09.063>.
- [3] R.J. Moon, M. Tilbrook, M. Hoffman, A. Neubrand, Al-Al₂O₃ Composites with Interpenetrating Network Structures: Composite Modulus Estimation, *J. Am. Ceram. Soc.* 88 (2005) 666–674, <https://doi.org/10.1111/j.1551-2916.2005.00115.x>.
- [4] A. Shaga, P. Shen, L.-G. Xiao, R.-F. Guo, Y.-B. Liu, Q.-C. Jiang, High damage-tolerance bio-inspired ZL205A/SiC composites with a lamellar-interpenetrated structure, *Materials Science and Engineering: A* 708 (2017) 199–207, <https://doi.org/10.1016/j.msea.2017.09.114>.
- [5] H.X. Peng, Z. Fan, J. Evans, Bi-continuous metal matrix composites, *Materials Science and Engineering: A* 303 (2001) 37–45.
- [6] A. Shaga, P. Shen, C. Sun, Q. Jiang, Lamellar-interpenetrated Al–Si–Mg/SiC composites fabricated by freeze casting and pressureless infiltration, *Materials Science and Engineering: A* 630 (2015) 78–84, <https://doi.org/10.1016/j.msea.2015.02.012>.
- [7] W. Shouren, G. Haoran, Z. Jingchun, W. Yingzi, Interpenetrating Microstructure and Properties of Si₃N₄/Al–Mg Composites Fabricated by Pressureless Infiltration, *Appl Compos Mater* 13 (2006) 115–126, <https://doi.org/10.1007/s10443-006-9015-x>.
- [8] O. Lavrentyeva DE102015202277A, 2015.
- [9] W.M. Kriven, J. Wang, D. Zhu, T. Fischer, S. Kirihara, *Developments in Strategic Ceramic Materials, first* (2015).
- [10] K.L. Scotti, D.C. Dunand, Freeze casting – A review of processing, microstructure and properties via the open data repository, FreezeCasting.net, *Progress in Materials Science* 94 (2018) 243–305, <https://doi.org/10.1016/j.pmatsci.2018.01.001>.
- [11] S. Skirl, M. Hoffman, K. Bowman, S. Wiederhorn, J. Rödel, Thermal Expansion Behavior and Macrostrain of Al₂O₃/Al Composites with Interpenetrating Networks, *Acta Metallurgica* 46 (1998) 2493–2499.
- [12] F.F. Lange, B.V. Velamakanni, A.G. Evans, Method for Processing Metal-Reinforced Ceramic Composites, *J American Ceramic Society* 73 (1990) 388–393.
- [13] M.H. Prado da Silva, A.F. Lemos, I.R. Gibson, J. Ferreira, J.D. Santos, Porous glass reinforced hydroxyapatite materials produced with different organic additives, *Journal of Non-Crystalline Solids* 304 (2002) 286–292, [https://doi.org/10.1016/S0022-3093\(02\)01036-0](https://doi.org/10.1016/S0022-3093(02)01036-0).
- [14] A. Lemos, J. Ferreira, Porous bioactive calcium carbonate implants processed by starch consolidation, *Materials Science and Engineering: C* 11 (2000) 35–40, [https://doi.org/10.1016/S0928-4931\(00\)00134-X](https://doi.org/10.1016/S0928-4931(00)00134-X).
- [15] Y. Sun, H. Zhang, A. Wang, H. Fu, Z. Hu, C. Wen, P. Hodgson, Compressive deformation and damage of Mg-based metallic glass interpenetrating phase composite containing 30–70 vol% titanium, *J. Mater. Res.* 25 (2010) 2192–2196, <https://doi.org/10.1557/JMR.2010.0272>.
- [16] J. Schukraft, D. Horny, K. Schulz, K. Weidenmann, 3d Modelling and Experimental Investigation on the Damage Behavior of an Interpenetrating Metal Ceramic Composite (Imcc) Under Compression, *SSRN Journal* (2021), <https://doi.org/10.2139/ssrn.3994161>.
- [17] T. Li, Y. Chen, L. Wang, Enhanced fracture toughness in architected interpenetrating phase composites by 3D printing, *Composites Science and Technology* 167 (2018) 251–259, <https://doi.org/10.1016/j.compscitech.2018.08.009>.
- [18] H. Chang, J. Binner, R. Higginson, Dry sliding wear behaviour of Al(Mg)/Al₂O₃ interpenetrating composites produced by a pressureless infiltration technique, *Wear* 268 (2010) 166–171, <https://doi.org/10.1016/j.wear.2009.07.014>.
- [19] A.J. Dolata, Tribological Properties of AlSi₁₂-Al₂O₃ Interpenetrating Composite Layers in Comparison with Unreinforced Matrix Alloy, *Materials (Basel)* 10 (2017), <https://doi.org/10.3390/ma10091045>.
- [20] M. Hoffman, S. Skirl, W. Pompe, J. Rödel, Thermal residual strains and stresses in Al₂O₃/Al composites with interpenetrating networks, *Acta Materialia* 47 (1999) 565–577, [https://doi.org/10.1016/S1359-6454\(98\)00367-X](https://doi.org/10.1016/S1359-6454(98)00367-X).
- [21] S. Roy, J. Gibmeier, V. Kostov, K.A. Weidenmann, A. Nagel, A. Wanner, Internal load transfer in a metal matrix composite with a three-dimensional interpenetrating structure, *Acta Materialia* 59 (2011) 1424–1435, <https://doi.org/10.1016/j.actamat.2010.11.004>.
- [22] S. Roy, J. Gibmeier, K.A. Weidenmann, A. Nagel, A. Wanner, Effect of Phase architecture on mechanical properties of interpenetrating metal/ceramic composites, in: W. Udomkitchdecha, T. Böllinghaus, A. Manonukul, J. Lexow (Eds.), *Materials Challenges and Testing for Manufacturing, Mobility, Biomedical*

Applications and Climate, Springer International Publishing, Cham, 2014, pp. 77–86.

- [23] S. Roy, J. Gibmeier, V. Kostov, K.A. Weidenmann, A. Nagel, A. Wanner, Internal load transfer and damage evolution in a 3D interpenetrating metal/ceramic composite, *Materials Science and Engineering: A* 551 (2012) 272–279, <https://doi.org/10.1016/j.msea.2012.05.016>.
- [24] Y. Sinchuk, S. Roy, J. Gibmeier, R. Piat, A. Wanner, Numerical study of internal load transfer in metal/ceramic composites based on freeze-cast ceramic preforms and experimental validation, *Materials Science and Engineering: A* 585 (2013) 10–16, <https://doi.org/10.1016/j.msea.2013.07.022>.
- [25] S. Roy, J. Gibmeier, A. Wanner, In situ Study of Internal Load Transfer in a Novel Metal/Ceramic Composite Exhibiting Lamellar Microstructure Using Energy Dispersive Synchrotron X-ray Diffraction, *Adv. Eng. Mater.* 11 (2009) 471–477, <https://doi.org/10.1002/adem.200800352>.
- [26] S. Roy, B. Butz, A. Wanner, Damage evolution and domain-level anisotropy in metal/ceramic composites exhibiting lamellar microstructures, *Acta Materialia* 58 (2010) 2300–2312, <https://doi.org/10.1016/j.actamat.2009.12.015>.
- [27] F. Delannay, 4.8 Thermal Stresses and Thermal Expansion in Metal Matrix Composites, in: *Comprehensive Composite Materials II*, Elsevier, 2018, pp. 213–241.
- [28] D.K. Balch, A. Mortensen, S. Suresh, Y.-L. Shen, T.J. Fitzgerald, V.J. Michaud, Thermal expansion of metals reinforced with ceramic particles and microcellular foams, *Metallurgical and Materials Transactions A* 27 (1996) 3700–3717, <https://doi.org/10.1007/BF02595462>.
- [29] S. Roy, A. Nagel, K.A. Weidenmann, Anisotropic thermal expansion behavior of an interpenetrating metal/ceramic composite, *Thermochemica Acta* 684 (2020), 178488, <https://doi.org/10.1016/j.tca.2019.178488>.
- [30] D. Horny, J. Schukraft, K.A. Weidenmann, K. Schulz, Numerical and Experimental Characterization of Elastic Properties of a Novel, Highly Homogeneous Interpenetrating Metal Ceramic Composite, *Adv. Eng. Mater.* (2020), <https://doi.org/10.1002/adem.201901556>.
- [31] J. Schukraft, C. Lohr, K.A. Weidenmann, 2D and 3D in-situ mechanical testing of an interpenetrating metal ceramic composite consisting of a slurry-based ceramic foam and AlSi10Mg, *Composite Structures* (2021), 113742, <https://doi.org/10.1016/j.compstruct.2021.113742>.
- [32] J. Schukraft, C. Lohr, K.A. Weidenmann, Mechanical characterization of an interpenetrating metal-matrix composite based on highly homogeneous ceramic foams, in: J.M. Hausmann, M. Siebert, A. von Hehl, K.A. Weidenmann (Eds.), *Hybrid 2020 Materials and Structures*, Sankt Augustin, 2020, pp. 33–39.
- [33] J. Schukraft, D. Horny, K. Schulz, K.A. Weidenmann, 3D modelling and experimental investigation on the damage behavior of an interpenetrating metal ceramic composite (IMCC) under compression, *Materials Science and Engineering: A* (2022), 143147, <https://doi.org/10.1016/j.msea.2022.143147>.
- [34] W. Sachse, *The Propagation of Elastic Waves in Anisotropic Solids and Their Use for Orientation and Elastic Constants Determination*, Report of the Department of Theoretical and Applied Mechanics (1973).
- [35] W.P. Mason, Physical Acoustics and the Properties of Solids, *J. Acoust. Soc. Am.* 28 (1956) 1197–1206, <https://doi.org/10.1121/1.1908593>.
- [36] M. Mah, D.R. Schmitt, Determination of the complete elastic stiffnesses from ultrasonic phase velocity measurements, *J. Geophys. Res.* 108 (2003), <https://doi.org/10.1029/2001JB001586>, ECV 6-1-ECV 6-11.
- [37] W.C. van Buskirk, S.C. Cowin, R.N. Ward, Ultrasonic measurement of orthotropic elastic constants of bovine femoral bone, *J. Biomech. Eng.* 103 (1981) 67–72, <https://doi.org/10.1115/1.3138262>.
- [38] L.C. Lynnworth, E.P. Papadakis, W.R. Rea, Ultrasonic Measurement of Phase and Group Velocity Using Continuous Wave Transmission Techniques, In: 1973 Ultrasonics Symposium, IEEE, 11/5/1973 - 11/7/1973, pp. 533–536.
- [39] C.S. Ting, W. Sachse, Measurement of ultrasonic dispersion by phase comparison of continuous harmonic waves, *J. Acoust. Soc. Am.* 64 (1978) 852–857, <https://doi.org/10.1121/1.382034>.
- [40] L.C. Lynnworth, W.R. Rea, E.P. Papadakis, Continuous wave transmission techniques for measuring ultrasonic phase and group velocities in dispersive materials and composites, *J. Acoust. Soc. Am.* 70 (1981) 1699–1703, <https://doi.org/10.1121/1.387235>.
- [41] A. Wanner, Elastic modulus measurements of extremely porous ceramic materials by ultrasonic phase spectroscopy, *Materials Science and Engineering: A* 248 (1998) 35–43, [https://doi.org/10.1016/S0921-5093\(98\)00524-3](https://doi.org/10.1016/S0921-5093(98)00524-3).
- [42] M. Nazeer, P. Jana, M.J. Oza, K.G. Schell, E.C. Bucharsky, T. Laha, S. Roy, Ultrasonic study of the elastic properties of functionally graded and equivalent monolithic composites, *Materials Letters* 323 (2022), 132594, <https://doi.org/10.1016/j.matlet.2022.132594>.
- [43] S. Roy, O. Stoll, K.A. Weidenmann, A. Nagel, A. Wanner, Analysis of the elastic properties of an interpenetrating AlSi12–Al₂O₃ composite using ultrasound phase spectroscopy, *Composites Science and Technology* 71 (2012) 962–968, <https://doi.org/10.1016/j.compscitech.2011.02.014>.
- [44] S. Roy, K.G. Schell, E.C. Bucharsky, P. Hettich, S. Dietrich, K.A. Weidenmann, A. Wanner, M.J. Hoffmann, Processing and Elastic Property Characterization of Porous SiC Preform for Interpenetrating Metal/Ceramic Composites, *J. Am. Ceram. Soc.* 95 (2012) 3078–3083, <https://doi.org/10.1111/j.1551-2916.2012.05347.x>.
- [45] S. Roy, K.G. Schell, E.C. Bucharsky, K.A. Weidenmann, A. Wanner, M.J. Hoffmann, Characterization of Elastic Properties in Porous Silicon Carbide Preforms Fabricated Using Polymer Waxes as Pore Formers, *J. Am. Ceram. Soc.* 96 (2013) 2269–2275, <https://doi.org/10.1111/jace.12341>.
- [46] C. Soyarslan, S. Bargmann, M. Pradas, J. Weissmüller, 3D stochastic bicontinuous microstructures: Generation, topology and elasticity, *Acta Materialia* 149 (2018) 326–340, <https://doi.org/10.1016/j.actamat.2018.01.005>.
- [47] M. Radovic, E. Lara-Curzio, L. Riestler, Comparison of different experimental techniques for determination of elastic properties of solids, *Materials Science and Engineering: A* 368 (2004) 56–70, <https://doi.org/10.1016/j.msea.2003.09.080>.
- [48] S. Höning, D. Koch, S. Weber, S. Etzold, T. Tonnesen, R. Telle, N. Traon, Evaluation of dynamic modulus measurement of C/C-SiC composites at different temperatures, *Int J Applied Ceramic Technology* 16 (2019) 1723–1733, <https://doi.org/10.1111/ijac.13293>.
- [49] E28 Committee, Test Method for Dynamic Youngs Modulus, Shear Modulus, and Poissons Ratio by Impulse Excitation of Vibration, ASTM International, West Conshohocken, PA.
- [50] T. Huber, H.P. Degischer, G. Lefranc, T. Schmitt, Thermal expansion studies on aluminium-matrix composites with different reinforcement architecture of {SiC} particles, *Composites Science and Technology* 66 (2006) 2206–2217, <https://doi.org/10.1016/j.compscitech.2005.12.012>.
- [51] DIN 51045:2005-08, Bestimmung der thermischen {Längenänderung} fester {Körper}, Berlin, 2005.
- [52] J. Cohen, *Statistical Power Analysis for the Behavioral Sciences*, Routledge (2013).
- [53] CES EduPack, GRANTA DESIGN, 2019.
- [54] EOS GmbH – Electro Optical Systems, EOS Aluminium AlSi10Mg, 2014. eos.info.
- [55] G. Castillo-Hernandez, M. Yasseri, B. Klobes, S. Ayachi, E. Müller, J. de Boor, Room and high temperature mechanical properties of Mg2Si, Mg2Sn and their solid solutions, *Journal of Alloys and Compounds* 845 (2020), 156205, <https://doi.org/10.1016/j.jallcom.2020.156205>.
- [56] L.Y. Jiang, T.T. Liu, C.D. Zhang, K. Zhang, T. Yang, C.C. Zhang, W.H. Liao, Thermal expansion behavior of CNT reinforced AlSi10Mg composite fabricated via laser powder bed fusion, *Mater. Res. Express* 6 (2019), 125806, <https://doi.org/10.1088/2053-1591/ab5b5b>.
- [57] R. Gumbleton, J.A. Cuenca, G.M. Klemencic, N. Jones, A. Porch, Evaluating the coefficient of thermal expansion of additive manufactured AlSi10Mg using microwave techniques, *Additive Manufacturing* 30 (2019), 100841, <https://doi.org/10.1016/j.addma.2019.100841>.
- [58] R. Bürgel, H.-J. Maier, T. Niendorf, *Handbuch Hochtemperatur-Werkstofftechnik: Grundlagen, Werkstoffbeanspruchungen, Hochtemperaturlegierungen und -beschichtungen*; mit 66 Tabellen, fourth., überarb. Auflage, Vieweg + Teubner, Wiesbaden, 2011.
- [59] M.F. Ashby, C. Gandhi, D. Taplin, Fracture-mechanism maps and their construction for f.c.c. metals and alloys, in: *Perspectives in Creep Fracture*, Elsevier, 1983, pp. 1–31.
- [60] H. Prielipp, M. Knechtel, N. Claussen, S.K. Streiffer, H. Müllejans, M. Rühle, J. Rödel, Strength and fracture toughness of aluminum/alumina composites with interpenetrating networks, *Materials Science and Engineering: A* (1995) 19–30.